The Astrophysical Journal, 944:229 (11pp), 2023 February 20 https://doi.org/10.3847/1538-4357/acb937

Near-infrared Polarization Charateristics of the Zodiacal Light Observed with DIRBE/COBE

Kohji Takimoto[1], Shuji Matsuura[2], Kei Sano[1], and Richard M. Feder[3]
[1] Department of Space Systems Engineering, School of Engineering, Kyushu Institute of Technology, Fukuoka 804-8550, Japan
takimoto.koji670@mail.kyutech.jp
[2] Department of Physics and Astronomy, School of Science, Kwansei Gakuin University, Hyogo 669-1337, Japan
[3] Department of Physics, California Institute of Technology, Pasadena, CA 91125, USA
Received 2022 December 13; revised 2023 January 19; accepted 2023 February 3; published 2023 February 28

Abstract

We report near-infrared polarization of the zodiacal light (ZL) measured from space by the Diffuse Infrared Background Experiment (DIRBE) on board the Cosmic Background Explorer in photometric bands centered at 1.25, 2.2, and 3.5 μm. To constrain the physical properties of interplanetary dust, we use DIRBE Weekly Sky Maps to investigate the solar elongation (ϵ), ecliptic latitude (β), and wavelength (λ) dependence of ZL polarization. We find that the polarization of the ZL varies as a function of ϵ and β, consistent with observed polarization at $\lambda = 550$ nm. While the polarization dependence on wavelength at $(\epsilon, \beta) = (90°, 0°)$ is modest (increasing from $17.7\% \pm 0.2\%$ at 1.25% μm to $21.0\% \pm 0.3\%$ at 3.5 μm), the variation is more pronounced at the north ecliptic pole ($23.1\% \pm 1.6\%$, $35.1\% \pm 2.0\%$, and $39.3\% \pm 2.1\%$ at 1.25, 2.2, and 3.5 μm, respectively). The variation in ZL polarization with wavelength is not explained by either Rayleigh scattering or absorptive particles larger than 10 μm.

Unified Astronomy Thesaurus concepts: Interplanetary dust (821); Zodiacal cloud (1845); Infrared Astronomical Satellite (785); Polarimetry (1278); Near infrared astronomy (1093)

1. Introduction

The zodiacal light (ZL) in the optical and the near-infrared is caused by sunlight scattered from interplanetary dust (IPD) particles in the solar system. Most recent studies support the hypothesis that the IPD is primarily derived from comets (Liou et al. 1995; Soderblom et al. 2002; Fernández et al. 2006; Nesvorny et al. 2010, 2011; Yang & Ishiguro 2015) and asteroids (Dermott et al. 1984; Schramm et al. 1989; Matsumoto et al. 1996; Tsumura et al. 2010), but further investigation is required to determine the relative contribution of the two. The typical radius of IPD particles is submicron to 100 μm (Grun et al. 1985; Reach 1988). Measurements of the ZL intensity and polarization provide important information that can help constrain the composition of the IPD. The Diffuse Infrared Background Experiment (DIRBE) on board the Cosmic Background Explorer (COBE) characterizes the ZL in the near-infrared (Hauser et al. 1991; Boggess et al. 1992; Silverberg et al. 1993). Kelsall et al. (1998) modeled the scattered-light component of the ZL intensity I_λ at wavelength λ as

$$I_\lambda = \int n(X, Y, Z) A_\lambda F_\lambda^\odot \Phi_\lambda(\Theta) ds, \quad (1)$$

where $n(X, Y, Z)$ is the three-dimensional density distribution of the IPD component, A_λ is the albedo, $F_\lambda^\odot$ is the solar flux, and $\Phi_\lambda(\Theta)$ is the phase function at scattering angle Θ. The ZL intensity observed in a given direction corresponds to the intensity integrated along the line of sight s. We show the ZL geometry observed in helio-ecliptic coordinates in Figure 1.

Zodiacal light scattered by IPD particles also exhibits systematic linear polarization. ZL polarization measurements are important for constraining IPD parameters such as size, shape, and constituent minerals, as well as for photometric and spectroscopic observations. The linear polarization P is defined as the difference in the degree of polarization intensity along the plane $I_\perp$ perpendicular to the scattering plane and $I_\parallel$ parallel to the scattering plane,

$$P = \frac{I_\perp - I_\parallel}{I_\perp + I_\parallel}.$$

P is positive if the polarization direction of the electric field is perpendicular to the scattering plane (Figure 1). Another source of near-infrared diffuse emission on a large scale is the Galactic plane, whose emission is due to stellar light, and which is polarized by less than 1% due to absorption by magnetically aligned dust particles (Jones & Gehrz 1990; Nagata 1990; Martin & Whittet 1990).

Most measurements are in the optical as opposed to the infrared, because near-infrared measurements are difficult to perform from the ground due to statistical and systematic errors from strong airglow by OH radicals in the upper atmosphere, which is several hundred times brighter than the ZL (Leinert et al. 1998). Several studies have been reported on ZL polarization measurements in the visible band. Figure 2 shows the results of recent ZL polarization observations from the ground and from space. Each observation was obtained in a different region of the sky. ZL polarization at optical wavelengths is observed by Astro 7 (Pitz et al. 1979), Skylab (Weinberg & Hahn 1980), Helios (Leinert & Blanck 1982), OSO-5 (Sparrow & Ney 1972), balloon-borne experiments (Van de Noord 1970), and ground-based telescopes (Wolstencroft & Brandt 1967), and with no strong trend in degree of polarization from $\lambda = 0.45$ to 0.8 μm.

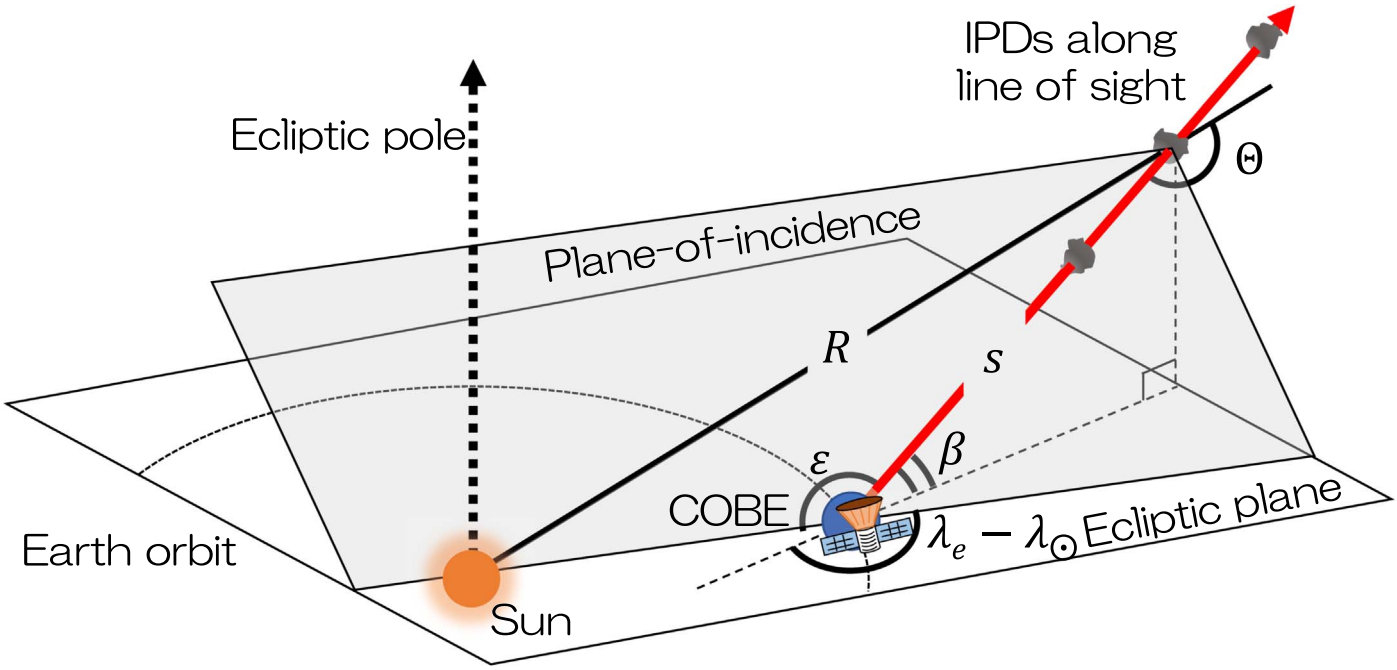

Figure 1. Geometric description of COBE observations with respect to the ecliptic latitude β, and the helio-ecliptic longitude, $(\lambda_e - \lambda_\odot)$, where λ_e is the ecliptic longitude and $\lambda_\odot$ is the ecliptic longitude of the Sun. The red arrow represents the line of sight from DIRBE, and s indicates the distance between DIRBE and an IPD grain. The observed ZL intensity corresponds to integrated light scattered by all IPD grains along DIRBE line of sight. The radial distance from the grain to the Sun is denoted by R, and the solar elongation is indicated by ϵ. The scattering angle is denoted by Θ.

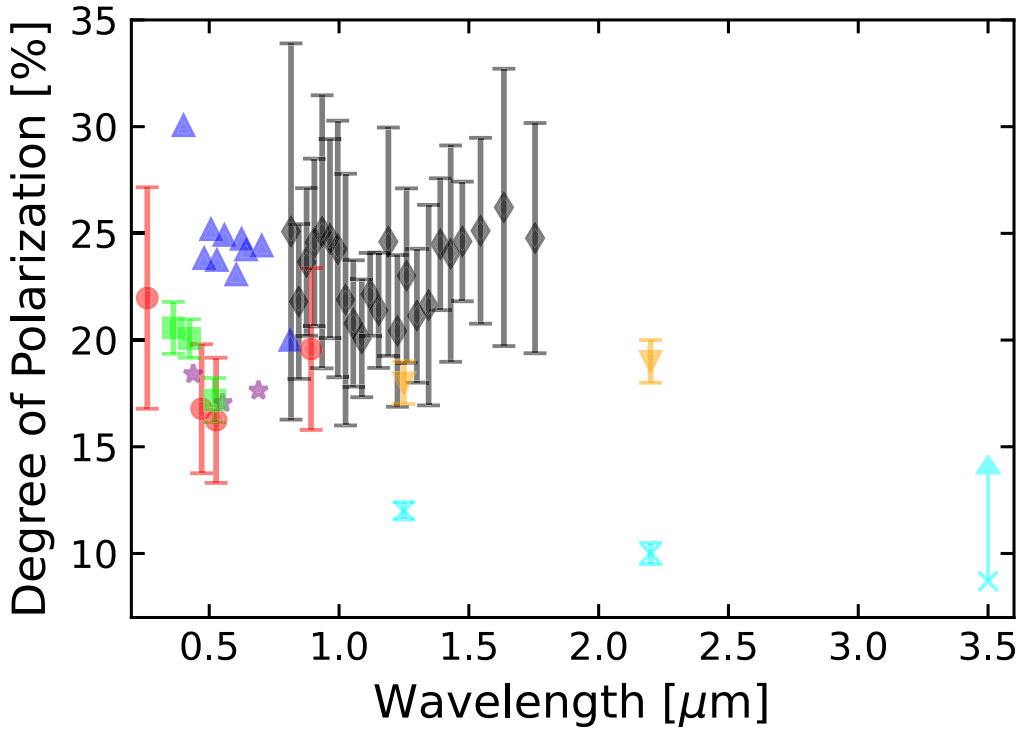

Figure 2. Zodiacal light polarization observed at different positions. Red circles: Astro 7 at $\epsilon = 30°$ (Pitz et al. 1979). Blue triangles: Skylab at the north celestial pole (Weinberg & Hahn 1980). Green squares: Helios at $\beta = 16°$, $\epsilon = 90°$ (Leinert & Blanck 1982). Purple stars: an average of three similar results (OSO-5 at $\epsilon = 90°$; Sparrow & Ney 1972; balloon observation at $\epsilon = 30°$; Van de Noord 1970; ground-based observation at $\epsilon = 39°$; Wolstencroft & Brandt 1967). Black diamonds: CIBER at the north ecliptic pole (Takimoto et al. 2022). Aqua crosses and orange inverted triangles: DIRBE at $\beta = 0°$, $\epsilon = 90°$ (Berriman et al. 1994; Takimoto et al.2022).

Lasue et al. (2020) reported a ZL polarization map at 550 nm based on data from Levasseur-Regourd (1996) and Leinert et al. (1998).

More recently, ZL polarization has been measured in the near-infrared. The ZL polarization spectrum from $\lambda = 0.8\ \mu$m to $1.8\ \mu$m observed by CIBER (Takimoto et al. 2022) also

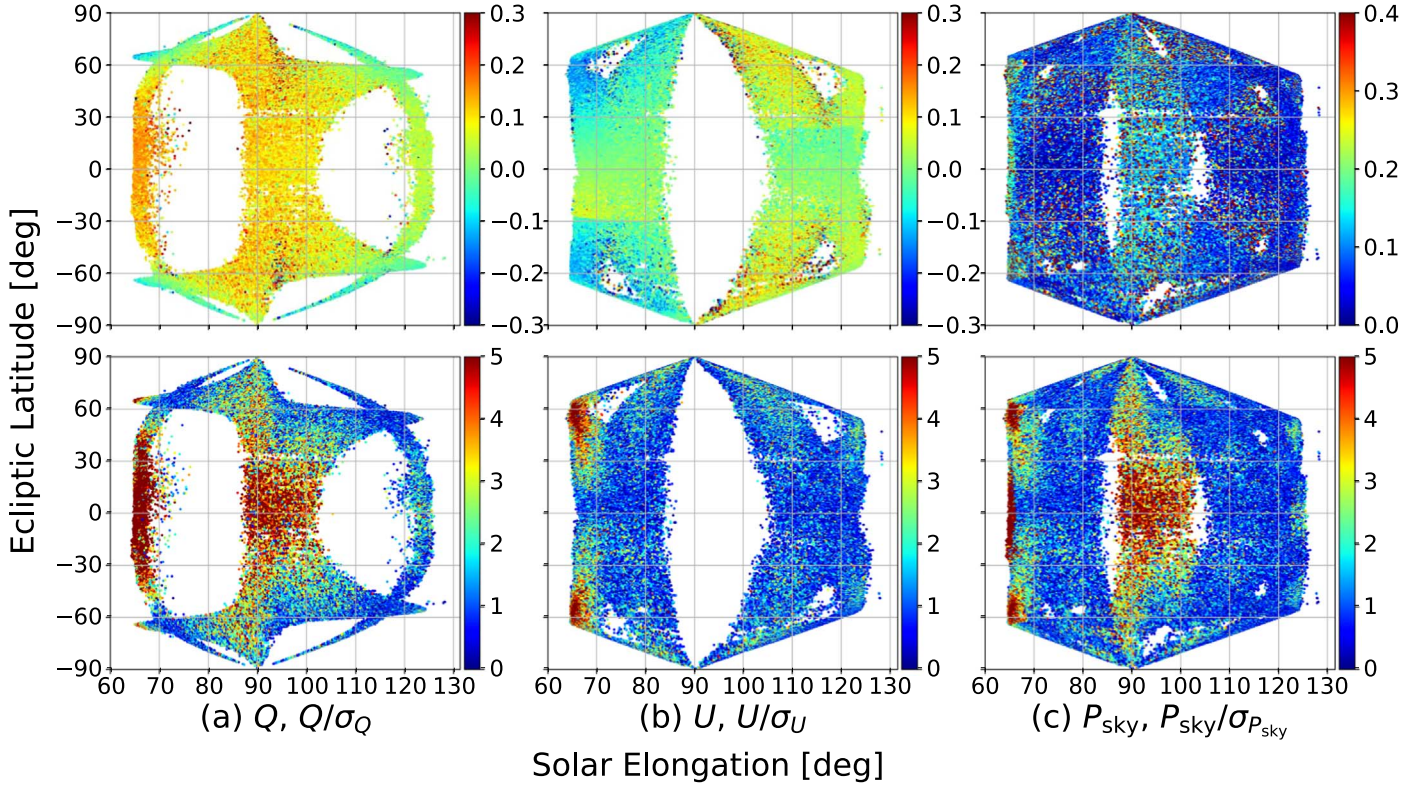

Figure 3. Top: sky maps of the Stokes parameters (a) Q, (b) U, and (c) degree of polarization of the sky brightness $P_{\rm sky}$ at 1.25 μm from 1989 December 11 to December 17. Bottom: S/N maps (a: Q/σ_Q, b: U/σ_U, and c: $P_{\rm sky}/\sigma_{P_{\rm sky}}$) with the same data as in the top row.

shows little dependence on wavelength. Note that because these observations probe different regions, the origin of IPD is considered to be different. In the case where a wavelength dependence is observed for ZL polarization at wavelengths even longer than 1.8 μm, the dominant scattering property of IPD has changed from geometrical-optical scattering to Mie scattering. Thus, it is possible that polarization observations in the near-infrared can constrain the particle radius of the dominant IPD causing ZL polarization.

DIRBE has performed the first and unique polarization survey of the diffuse sky at $\lambda = 1.25$, 2.2, and 3.5 μm. Berriman et al. (1994) reported the ZL polarization in the ecliptic plane (ecliptic latitude $\beta = 0°$) at solar elongation $\epsilon = 90°$ using only one week of observations, but diffuse radiation and starlight were not subtracted in all wavelength bands, and the 3.5 μm results include a thermal radiation component of the ZL. Takimoto et al. (2022) also estimated the ZL polarization at 1.25 and 2.2 μm from the DIRBE result presented in Berriman et al. (1994), but the ZL polarization shows little dependence on λ after other diffuse light sources are considered (Arendt et al. 1998; Cambrésy et al. 2001; Girardi et al. 2005; Skrutskie et al. 2006; Tsumura et al. 2013; Arai et al. 2015).

In this paper, we report a new dependence on ϵ , β , and λ of the ZL polarization in the near-infrared measured from space by DIRBE. We obtain the ZL polarization using 41 weeks of DIRBE observations and make near-infrared ZL polarization maps for the three bands from 1.25 to 3.5 μm. Our careful data processing suggests that most of the DIRBE polarimetric observations are data with a low signal-to-noise ratio (S/N), which is the reason that these data have not been analyzed for many years. Therefore, we carefully extracted only high SNR data, and we use the data around $\epsilon = 90°$ to study the characteristics of ZL polarization.

2. Method

2.1. DIRBE Weekly Sky Maps

DIRBE is one of three instruments on board the COBE satellite (Hauser et al. 1991; Boggess et al. 1992; Silverberg et al. 1993). In addition to photometric observations, DIRBE was designed to make measurements of linear polarization in three bands centered at 1.25, 2.2, and 3.5 μm. The DIRBE optical axis is oriented at 30° from the COBE spacecraft spin axis and observed half of the sky each day at solar elongation angles ranging from $\epsilon = 64°$ to 124°. The weekly sky maps[4] consist of 41 files, one per week of optimized operation of the cryogenic mission from 1989 November 24 to 1990 September 21 (Hauser et al. 1998). For telemetry data from DIRBE, data reduction and absolute calibration of the available maps have already been done by the DIRBE team. The weekly sky maps give Stokes Q and U parameters at 1.25, 2.2, and 3.5 μm. The Stokes parameters for each band are averages of the individual Q and U observations, weighted by their measurement uncertainties. The standard deviations of the weighted mean values of the Stokes parameters are σ_Q and σ_U, respectively. Q is the component parallel (positive) or perpendicular (negative) to the local line of ecliptic longitude, and U is the component 45° E (positive) or 45° W (negative) to the local line of ecliptic longitude. The degree of polarization P and its standard deviation σ_P are calculated using Q, U, σ_Q, and σ_U as

$$P = \begin{cases} Q\cos 2\theta + U\sin 2\theta, & \text{if both Q and U exist} \\ Q/\cos 2\theta, & \text{if only Q exists} \\ U/\sin 2\theta, & \text{if only U exists} \end{cases} \quad (2)$$

[4] https://lambda.gsfc.nasa.gov/product/cobe/dirbe_cwm_data_get.html

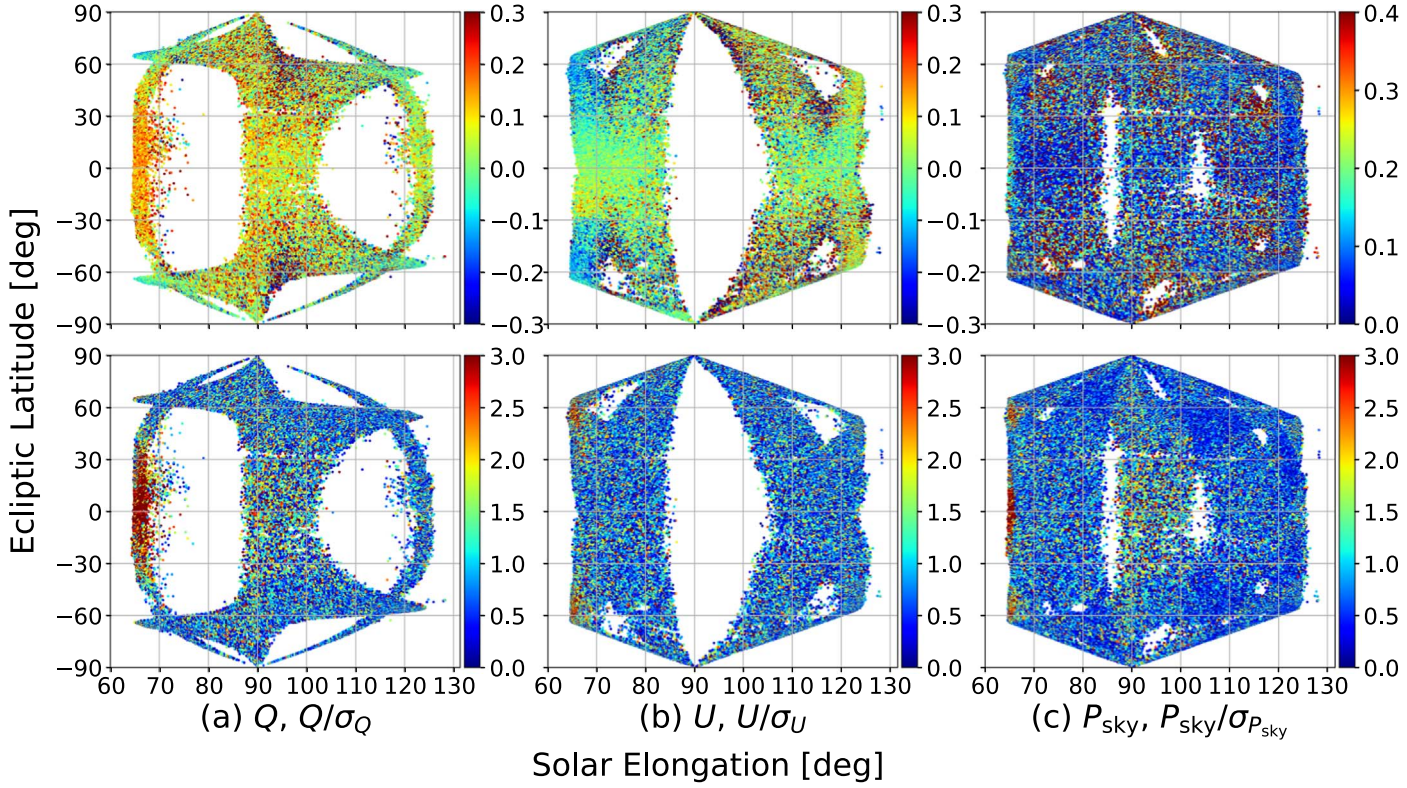

Figure 4. Same as Figure 3, but at 2.2 μm from 1989 December 11 to December 17.

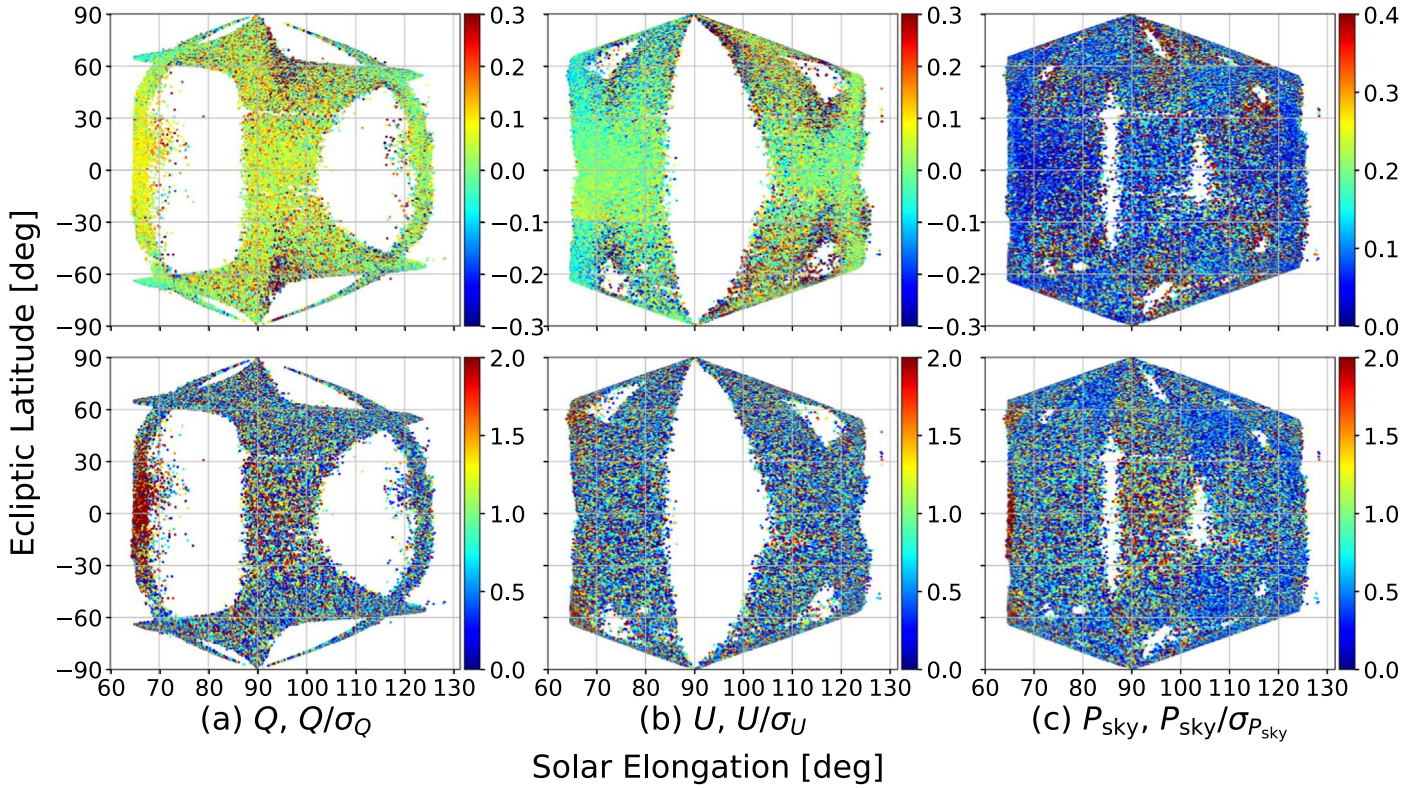

Figure 5. Same as Figure 3, but at 3.5 μm from 1989 December 11 to December 17.

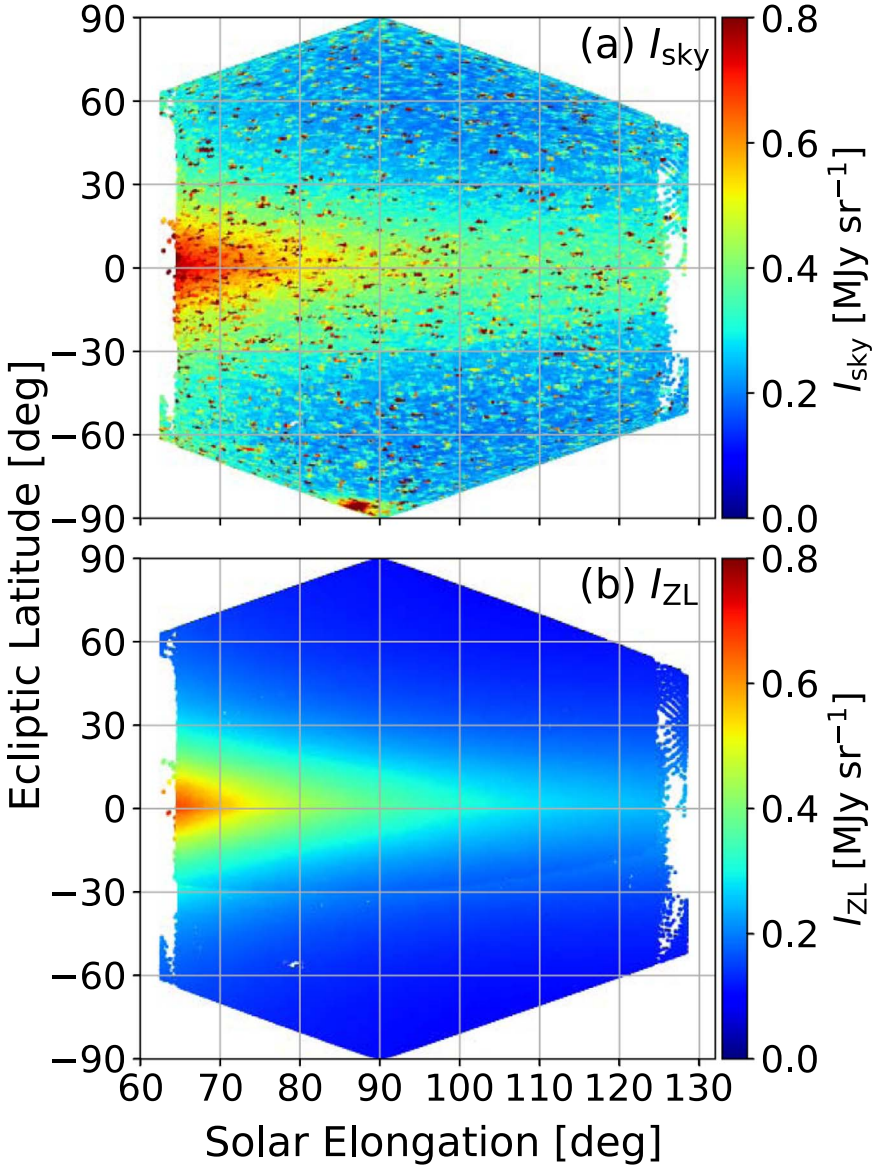

Figure 6. (a) Intensity map obtained from the DIRBE intensity channel at 1.25 μm from 1989 December 11 to December 17. (b) ZL intensity map estimated by DIRBE IPD model (Kelsall et al. 1998) at 1.25 μm.

$$\sigma_P = \begin{cases} P\sqrt{\left(\frac{\sigma_Q}{Q}\right)^2 + \left(\frac{\sigma_U}{U}\right)^2}, & \text{if both Q and U exist} \\ P\frac{\sigma_Q}{Q}, & \text{if only Q exists} \\ P\frac{\sigma_U}{U}, & \text{if only U exists} \end{cases} \quad (3)$$

where θ is the orientation of the polarizer, defined as the angle between the polarizer axis and the local meridian. θ is computed in the range $[-90°, +90°]$. Since P is always a positive quantity, unlike Q and U, which can be positive or negative, the naive estimate $P = \sqrt{Q^2 + U^2}$ is biased for low S/N data. σ_P tends to be larger when P is evaluated from both Q and U than when P is evaluated using only Q because of the large σ_U in the data. However, the difference in P is smaller than 10%. The mean observation time and mean solar elongation angle for each sky region are also recorded in the weekly sky maps. Further information about the data processing of the DIRBE polarization can be found in Hauser et al. (1998).

All 41 weekly sky map files have file extensions in FITS format. A quadrilateralized spherical projection and a quadtree pixelization scheme were adopted for all COBE sky maps, including the DIRBE maps. The COBE quadrilateralized spherical cube (CSC) is an approximately equal-area projection in which the celestial sphere is projected onto an inscribed cube. The coordinate system is Geocentric Ecliptic J2000. An ancillary information file called `DIRBE_SKYMAP_INFO.FITS` explains the quadtree scheme, which relates CSC pixel numbers to (x, y) positions within the quadsphere cube faces and tabulates the ecliptic J2000, Galactic (l, b) and equatorial J2000 coordinates corresponding to the DIRBE pixel centers. This file may be obtained from the DIRBE ancillary data products page.[5]

[5] https://lambda.gsfc.nasa.gov/product/cobe/dirbe_ancil_qs_get.html

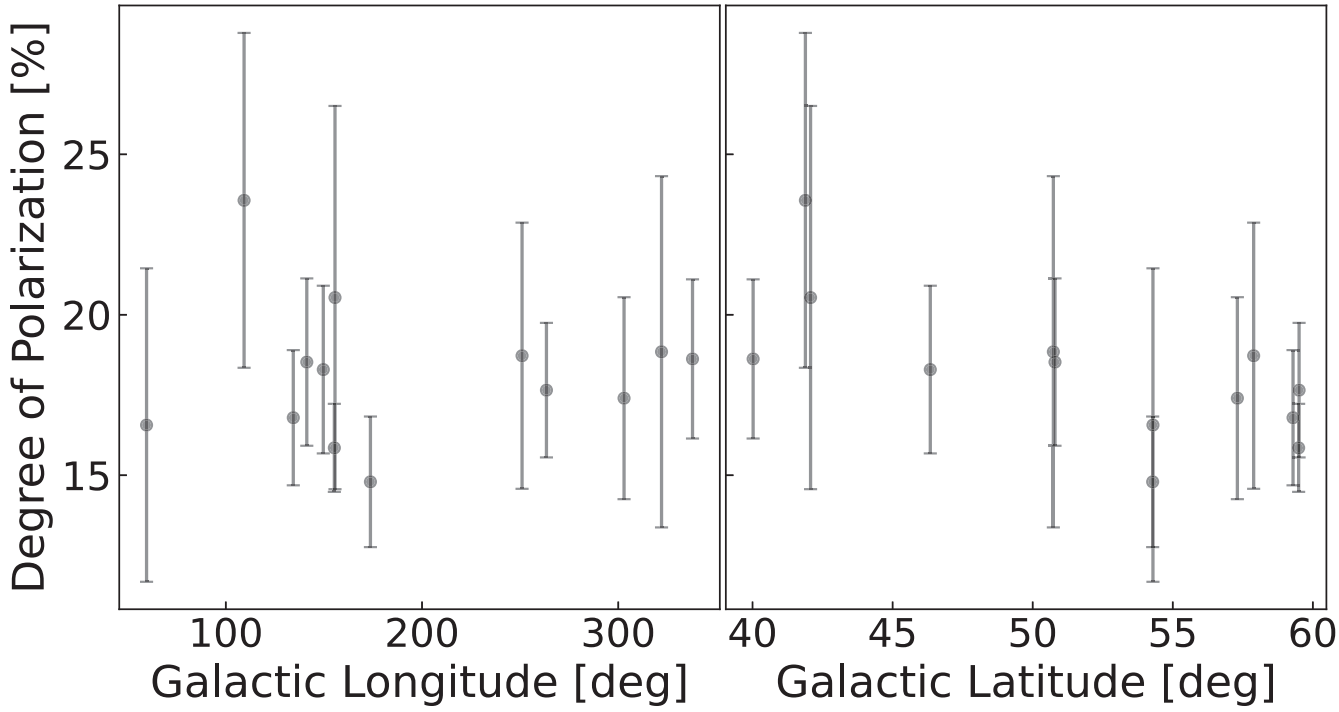

Figure 7. The Galactic coordinate dependence of $P_{\rm ZL}$ at $\lambda = 1.25$ μm and $(\epsilon, \beta) = (90^\circ, 0^\circ)$. Plots are weekly results, smoothed by a weighted average of the region averaged over one square degree.

To apply data cuts and check for systematics and dependences, we convert into several coordinate systems. After converting the maps to ecliptic, Galactic, and equatorial coordinates, the following processing is applied to each map. Only data in the high Galactic latitude region ($|b| > 30^\circ$) are extracted because data in the Galactic plane are not suitable for studying ZL polarization. In addition, we exclude data obtained when the DIRBE line of sight approached certain solar system objects to avoid contaminating the data by light from moving objects. We also remove noisy data in regions with fewer than 10 observations per week, when the calculation of the Stokes parameters by robust fitting part of DIRBE original data processing fails, or when the processing of polarization ratios fails to produce Q or U values. The degree of polarization derived by Equation (2) using the raw DIRBE data is the ratio of the intensity of the total sky to the intensity of the polarization component. The polarization of the sky brightness, $P = P_{\rm sky}$, can be written as

$$P_{\rm sky} = \frac{I_{\rm pol}}{I_{\rm sky}}, \tag{4}$$

where $I_{\rm pol}$ is the intensity of the polarized light component from the DIRBE polarization channel, and $I_{\rm sky}$ is the intensity obtained from the DIRBE intensity channel.

Figures 3–5 represent sky maps of Stokes parameters and the degree of polarization of the sky brightness from 1.25 to 3.5 μm for a week. $P_{\rm sky}$ map at 1.25 μm for a solar elongation below 70° or near 90° is more reliable than other regions because the S/N ($P_{\rm sky}/\sigma_{P_{\rm sky}}$) is more than three. Uncertainties on the polarization depend on the coverage map in both Q and U. Since the ZL brightness decreases toward longer wavelengths in the near-infrared, the same as for the solar spectrum, the S/Ns of the observed data at 2.2 and 3.5 μm are lower than those at 1.25 μm. The total number of $P_{\rm sky}$ data calculated for all weekly data is 1,624,852 at 1.25 μm, 2,645,893 at 2.2 μm, and 2,645,681 at 3.5 μm. The difference in the total number is due to unexplained malfunctions in each polarization channel, especially in b channel, where 1.25 μm is inoperative for about 35% of the observation period. This channel is especially noisy for observations in which the Moon is visible in the viewing swath.

2.2. Polarization Measurement

From measurements of the polarization on the sky and from surface brightness measurements, we derive estimates of the ZL polarization, $P_{\rm ZL}$. We assume that the polarization components of the other diffuse radiation are negligible compared to the ZL. $I_{\rm sky}$ denotes the integrated surface brightness from ZL, $I_{\rm ZL}$, along with contributions from bright point sources and other diffuse radiation, including diffuse Galactic light (DGL), integrated starlight (ISL), and the extragalactic background light (EBL). Bright galaxies are also a source of astrophysical noise for the DIRBE measurement. In addition, $I_{\rm sky}$ at 3.5 μm is contaminated by the thermal emission component of the ZL from IPD particles. The corrected polarization, $P_{\rm ZL}$, is expressed as

$$P_{\rm ZL} = P_{\rm sky}\frac{I_{\rm sky}}{I_{\rm ZL}}, \tag{5}$$

where $I_{\rm ZL}$ is the ZL intensity, which is only sunlight scattering, at each wavelength derived in Equation (1) (Kelsall et al. 1998). Figure 6 shows sky maps of $I_{\rm sky}$ and $I_{\rm ZL}$ at 1.25 μm for a week. The $I_{\rm sky}$ map shows the contribution of stars and the Large Magellanic Cloud ($(\epsilon, \beta) \sim (88^\circ, -85^\circ)$). $I_{\rm sky}$ is also higher than $I_{\rm ZL}$ in all regions due to other diffuse light. We check for temporal variation in the polarization before averaging the results across all weeks. Figure 7 shows the Galactic coordinate dependence of $P_{\rm ZL}$ around $\epsilon = 90^\circ$ at

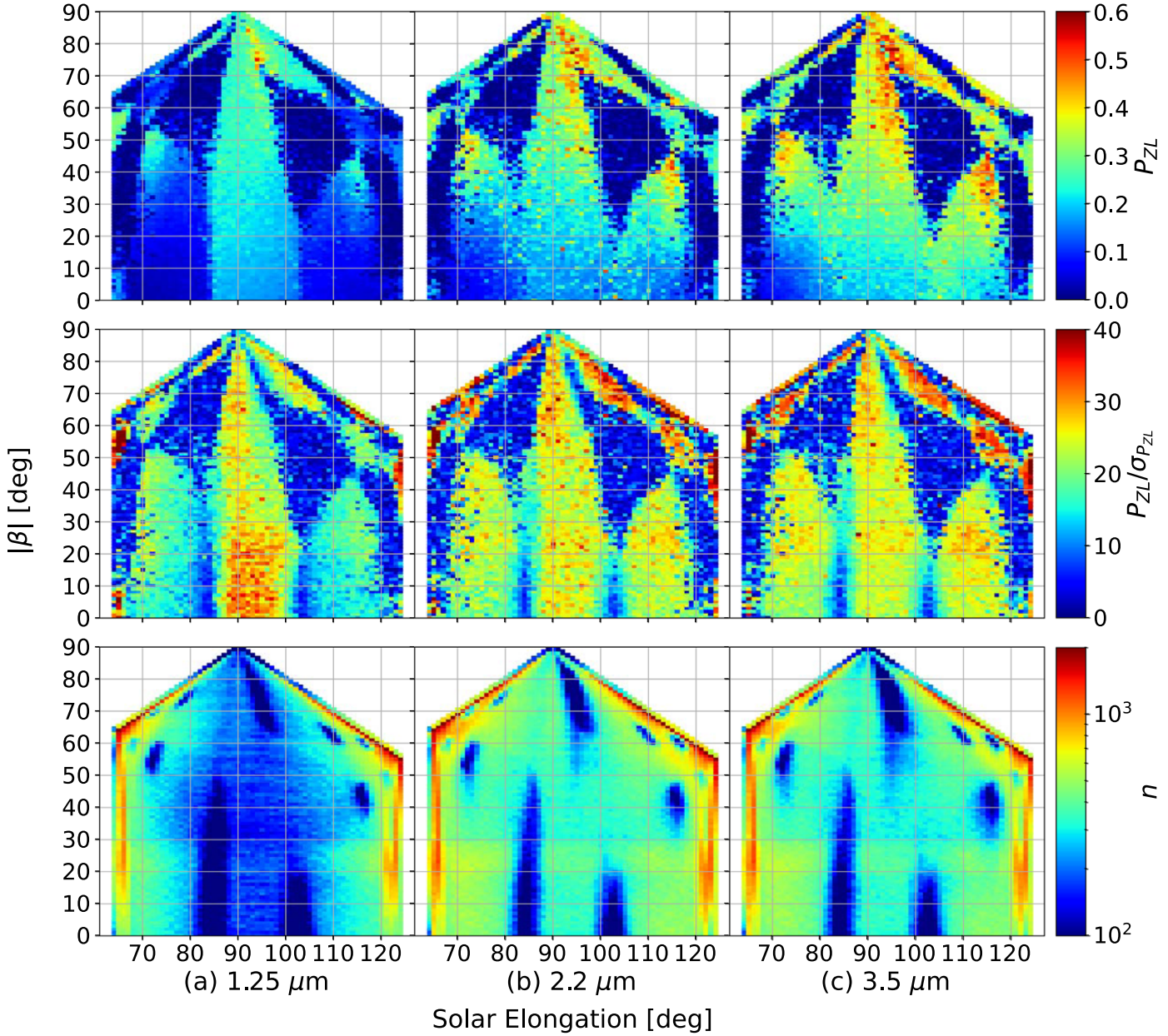

Figure 8. Top: zodiacal light polarization map for each wavelength(a: 1.25 μm, b: 2.2 μm, c: 3.5 μm) calculated by weighted average per one square degree. Middle: S/N map. Bottom: number of ZL in the polarization data map.

$\beta = 0°$. The standard deviation across weeks in this region is 2.11%. The combined data are consistent up to the measurement uncertainty. Figure 8 shows the $P_{\rm ZL}$ map, the $P_{\rm ZL}/\sigma_{P_{\rm ZL}}$ map, and the number of $P_{\rm ZL}$ data, and the n map at each wavelength. Each map is smoothed by a weighted mean of regions over one square degree, with no north–south distinction of ecliptic latitude, by using data from all weekly observations. $\sigma_{P_{\rm ZL}}$ is the standard deviation of the weighted mean of the degree of polarization. Around $\epsilon = 90°$, the $P_{\rm ZL}$ map at 1.25 μm shows a high S/N of more than 25, despite the small n. Even though $\sigma_{P_{\rm ZL}}$ is inversely proportional to the square root of n, the high S/N confirms that this region is more reliable than other regions. As already mentioned in Section 2.1, the standard deviations, such as σ_Q, σ_U, and $\sigma_{P_{\rm sky}}$, near the region where neither the Stokes parameter Q nor U exists, are larger than those in other regions. Therefore, even if n is large and $P_{\rm ZL}/\sigma_{P_{\rm ZL}}$ is high, the reliability is low in certain regions (e.g., $(\epsilon, \beta) = (115°, \pm 30°)$, $(95°, \pm 60°)$, and $(75°, \pm 45°)$). For these reasons, we use only the region around $\epsilon = 90°$ to study the dependence on ϵ, β, and λ dependence.

3. Results and Discussions

3.1. Solar Elongation Dependence

Since the Stokes parameter U is zero in the ecliptic plane, the dependence on ϵ of $P_{\rm ZL}$ is valid only in the measurement region of the Stokes parameter Q. Figure 9 shows the dependence on ϵ of $P_{\rm ZL}$ around $\epsilon = 90°$ at $\beta = 0°$. $P_{\rm ZL}$ near the ecliptic plane

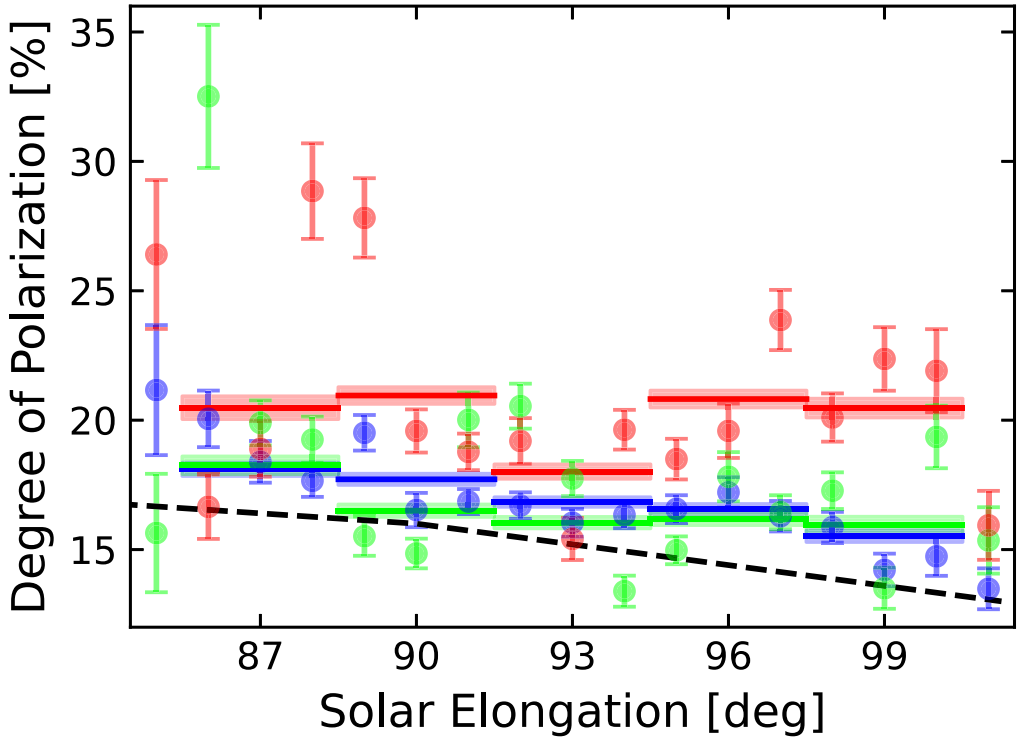

Figure 9. The solar elongation dependence of $P_{\rm ZL}$ at $\beta = 0°$. The filled circles are the result of this work, smoothed by a weighted average of the region averaged over one square degree (blue: 1.25 μm, green: 2.2 μm, and red: 3.5 μm). The solid lines are the result of this work, smoothed by a weighted mean of regions over three square degrees. The error bars and the shaded regions indicate the standard deviation of the weighted mean of the degree of polarization. The dashed line represents the ZL polarization at $\lambda = 550$ nm (Levasseur-Regourd 1996; Leinert et al. 1998).

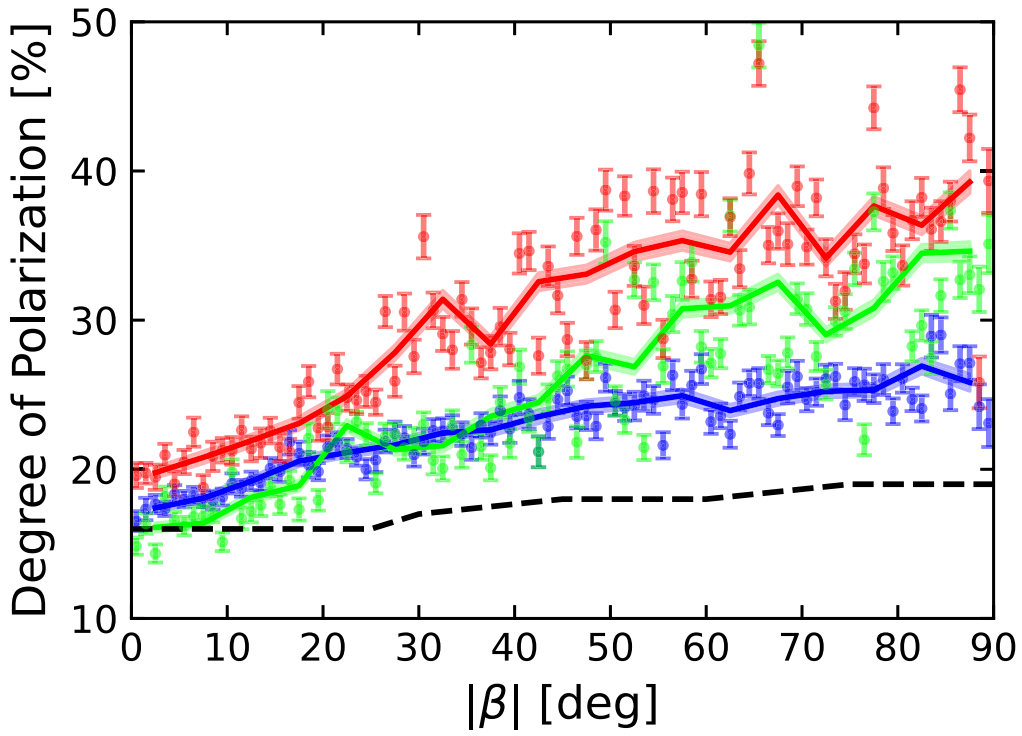

Figure 10. The dependence on ecliptic latitude of $P_{\rm ZL}$ at $\epsilon = 90°$. The filled circles are the result of this work, smoothed by a weighted average of the region averaged over one square degree (blue: 1.25 μm, green: 2.2 μm, and red: 3.5 μm). The solid lines are the result of this work, smoothed by a weighted mean of regions averaged over five square degrees. The error bars and the shaded regions indicate the standard deviation of the weighted mean of the degree of polarization. The dashed line represents the ZL polarization at $\lambda = 550$ nm (Levasseur-Regourd 1996; Leinert et al. 1998).

shows little dependence on wavelength; it differs by only a few percent. At $\lambda = 1.25$ μm, $P_{\rm ZL}$ tends to decrease as ϵ increases, which can be explained by the fact that the degree of polarization generally decreases with increasing scattering angle above 90° (Giese et al. 1978). This trend is also consistent with the degree of polarization observed from Earth

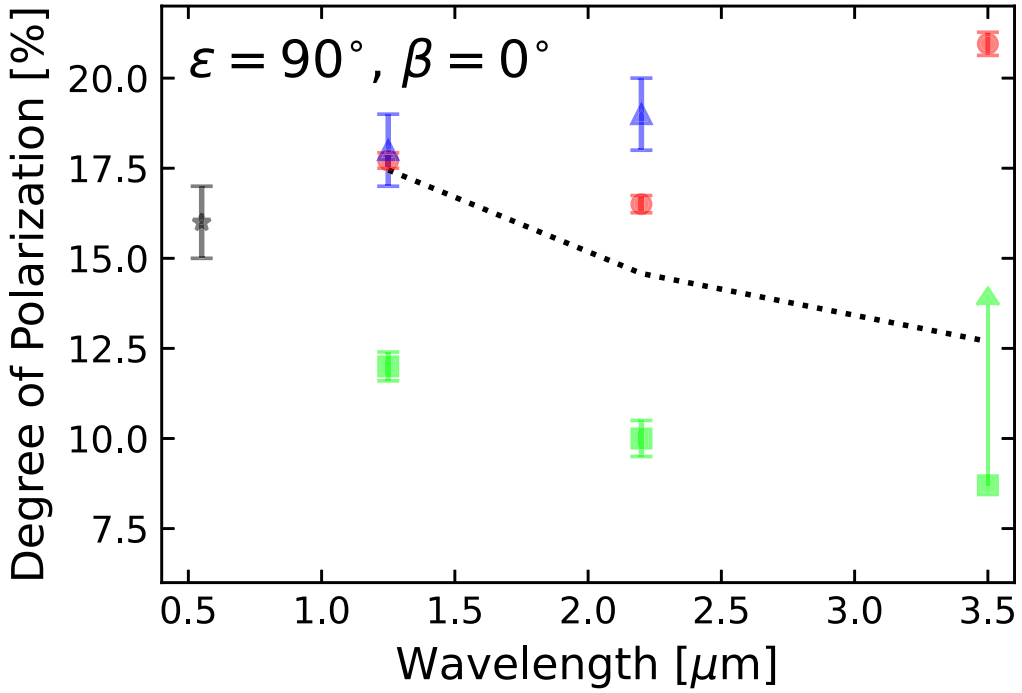

Figure 11. The wavelength dependence of $P_{\rm ZL}$ at $\epsilon = 90°$ and $\beta = 0°$. The red circles are the results of this work. The error bars indicate the standard deviation of the weighted mean of the degree of polarization. The degree of polarization calculated by Berriman et al. (1994) is shown as green squares (1.25 and 2.2 μm) and the arrow (lower limit at 3.5 μm). The blue triangles are the results calculated by Takimoto et al. (2022). The black star indicates the ZL polarization at 0.55 μm (Levasseur-Regourd 1996). The dotted line represents the degree of polarization calculated by the geometrical-optical scattering with graphite (Draine & Lee 1984).

at $\lambda = 550$ nm (Levasseur-Regourd 1996; Leinert et al. 1998). On the other hand, there is no significant dependence on ϵ of $P_{\rm ZL}$ at 2.2 and 3.5 μm because the standard deviation of the data is large. Another factor may be that the scattering angle dependence on the degree of polarization of IPD is different in the near-infrared. As the wavelength increases, $P_{\rm ZL}$ increases, and the dependence on ϵ becomes weak not because of a real decorrelation, but as a result of noisy observations.

3.2. Dependence on Ecliptic Latitude

We compare the degree of polarization from the ecliptic plane to the ecliptic pole at $\epsilon = 90°$. $P_{\rm ZL}$ as a function of the ecliptic latitude β at $\epsilon = 90°$ is shown in Figure 10. At all observed wavelengths, $P_{\rm ZL}$ tends to increase as $|\beta|$ increases. This trend is also consistent with $P_{\rm ZL}$ at $\lambda = 550$ nm. This dependence on β can be explained by the fact that as $|\beta|$ increases, there are fewer IPDs farther away in the line-of-sight direction, and the majority of $P_{\rm ZL}$ is produced by IPDs near the Earth. The dependence on β is larger at longer wavelengths, with $P_{\rm ZL}$ at 3.5 μm about twice as large as that at 550 nm in the ecliptic pole region.

3.3. Wavelength Dependence

Figure 11 shows $P_{\rm ZL}$ as a function of the wavelength λ at $\epsilon = 90°$ and $\beta = 0°$. $P_{\rm ZL}$ at 1.25, 2.2, and 3.5 μm are $17.7\% \pm 0.2\%$, $16.5\% \pm 0.2\%$, and $21.0\% \pm 0.3\%$. Our results show that there is little dependence on wavelength of $P_{\rm ZL}$ near the ecliptic plane from the visible to the near-infrared. Compared to the average value from Berriman et al. (1994), our results are higher by more than 5%. On the other hand, the degree of polarization at 1.25 and 2.2 μm, removed starlight, and other contributions by Takimoto et al. (2022) are consistent with this work. The polarization due to graphite (Draine & Lee 1984) with particle radii greater than 10 μm, based on Mie theory calculations, shows a tendency to decrease toward longer wavelengths, different from our results.

$P_{\rm ZL}$ as a function of the wavelength λ in the NEP field is shown in Figure 12. Our result at $\lambda = 1.25$ μm is $P_{\rm ZL} = 23.1\% \pm 1.6\%$, consistent with CIBER results. In addition, our work at $\lambda = 2.2$ and 3.5 μm shows $P_{\rm ZL} = 35.1\% \pm 2.0\%$ and $39.3\% \pm 2.1\%$, respectively. Our results suggest that $P_{\rm ZL}$ tends to increase toward longer wavelengths in the visible to the near-infrared. From CIBER observations, the polarization properties of ZL at 1.25 μm can be explained if the IPD particles are dominated by absorptive materials with a particle radius of 1 μm or larger (Takimoto et al. 2022). On the other hand, a candidate IPD particle that provides a high degree of polarization at wavelengths longer than 2.2 μm requires a size equal to or smaller than the wavelength. Absorptive particles larger than 10 μm in diameter exhibit geometrical-optical scattering characteristics. Thus, when particles larger than 10 μm dominate, the ZL polarization indicates a decreasing trend toward longer wavelengths, so the results measured by DIRBE cannot be reproduced. Therefore, it is suggested that absorptive particles with a radius between 1 and 10 μm dominate the polarization properties. Another candidate is porous silicate grains with a power-law number distribution by mass of $dn/d\log m \propto m^{\alpha}$, where $\alpha = -0.56$ (Berriman et al. 1994). This is similar to the model that Lisse et al. (1994) found to be applicable to comets. Therefore, it is suggested that the IPD drifting in the high ecliptic latitude region is cometary dust composed of porous silicates. Table 1 summarizes the observation fields and the degree of polarization of the ZL.

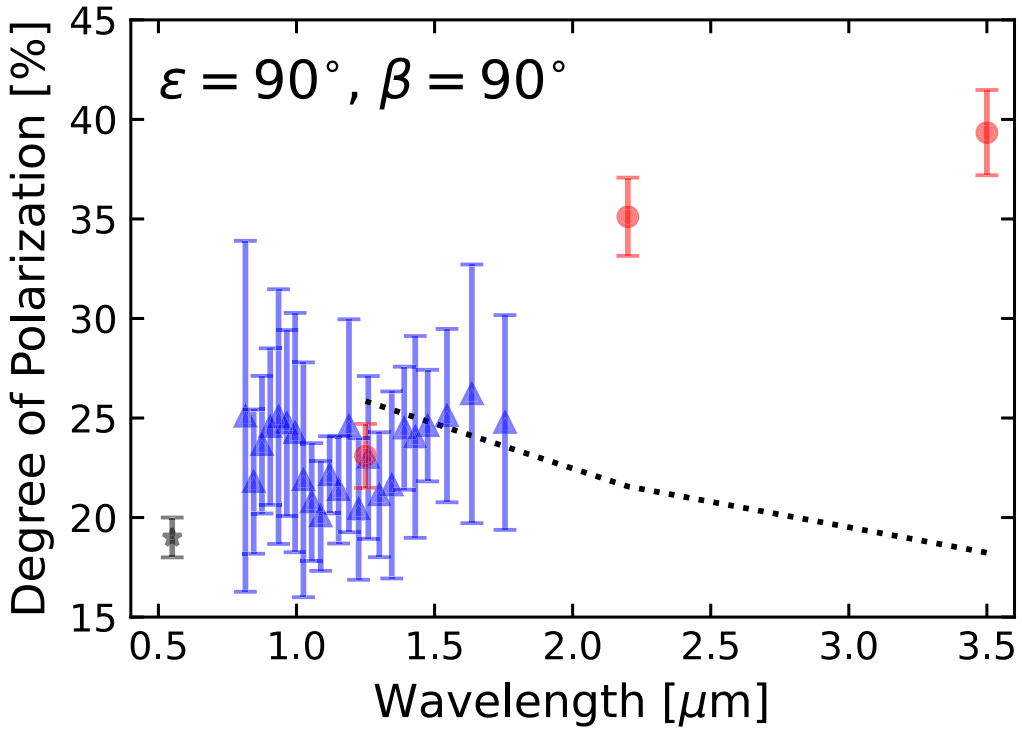

Figure 12. The wavelength dependence of P_{ZL} at the NEP field. The red circles are the results of this work. The error bars represent the standard deviation of the weighted mean of the degree of polarization. The blue triangles are the ZL polarization spectrum measured with CIBER (Takimoto et al. 2022). The black star indicates the ZL polarization at 0.55 μm (Levasseur-Regourd 1996). The dotted line represents the degree of polarization calculated by Mie scattering using graphite with a particle radius of 10 μm (Draine & Lee 1984).

Table 1
Near-infrared Polarization of the ZL Observed with DIRBE

Wavelength λ (μm)	Ecliptic Lat. β (deg)	Solar Elong. ϵ (deg)	Degree of Pol. P_{ZL} (%)
1.25	0	90	17.7 ± 0.2
	90	90	23.1 ± 1.6
2.2	0	90	16.5 ± 0.2
	90	90	35.1 ± 2.0
3.5	0	90	21.0 ± 0.3
	90	90	39.3 ± 2.1

The polarization properties of ZL obtained with DIRBE can be a crucial tool for constraining the various properties of IPD. However, we cannot determine the origin of IPDs from our data alone. Future work is necessary to better constrain the properties of the IPD particles. We need to devise a new spatial distribution model for IPD that includes an isotropic component of the ZL (Sano et al. 2020). The polarization properties of IPD particles must be investigated in more detail. More theoretical modeling of IPD scattering is needed to determine the origin of IPD. Future model simulations will need to carefully consider the wavelength-specific scattering properties of the constituent minerals to improve our understanding of the structure and physical properties of IPD. In addition, incorporating details of the complex particle shape and size distribution into the model should make a reproduction of the observed ZL polarization possible. Further polarization data at solar elongation, which were not observed in DIRBE, are needed to limit the composition of IPD. Forward scattering ($\Theta < 90°$) shows characteristic composition-dependent scattering properties and is effective for validating compositional models of IPDs. Therefore, near-infrared ZL polarization observations at $\epsilon < 60°$ are especially necessary to capture forward-scattering components.

4. Conclusion

We described the near-infrared polarization of the ZL measured from space by DIRBE/COBE in the discrete photometric bands of 1.25, 2.2, and 3.5 μm. To make ZL polarimetric maps using the all data from the DIRBE weekly sky maps, we replaced the sky intensity, which includes contributions from starlight and other sources from observations, with a ZL intensity model. These maps show the characteristics of different S/Ns for each sky region and wavelength of observation. New analysis in terms of solar elongation, ecliptic latitude, and wavelength suggests that the ZL polarization of the near-infrared can be explained by an absorptive particle model with a size of a few microns. For the 1.25 μm ZL polarization map, the degree of polarization of the NEP region is consistent with CIBER observations, and the degree of polarization near the ecliptic plane is also comparable to DIRBE observations, which were estimated using different methods. More detailed investigation of the particle properties is needed in the future.

COBE is supported by NASA's Astrophysics Division. The Goddard Space Flight Center (GSFC), under the scientific guidance of the COBE Science Working Group, is responsible for the development and operation of COBE.

ORCID iDs

Kohji Takimoto https://orcid.org/0000-0002-8405-9549
Shuji Matsuura https://orcid.org/0000-0002-5698-9634
Kei Sano https://orcid.org/0000-0002-6468-8532
Richard M. Feder https://orcid.org/0000-0002-9330-8738

References

Arai, T., Matsuura, S., Bock, J., et al. 2015, ApJ, 806, 69
Arendt, R. G., Odegard, N., Weiland, J. L., et al. 1998, ApJ, 508, 74
Berriman, G. B., Boggess, N. W., Hauser, M. G., et al. 1994, ApJL, 431, L63
Boggess, N. W., Mather, J. C., Weiss, R., et al. 1992, ApJ, 397, 420
Cambrésy, L., Reach, W. T., Beichman, C. A., & Jarrett, T. H. 2001, ApJ, 555, 563
Dermott, S. F., Nicholson, P. D., Burns, J. A., & Houck, J. R. 1984, Natur, 312, 505
Draine, B. T., & Lee, H. M. 1984, ApJ, 285, 89
Fernández, Y. R., Campins, H., Kassis, M., et al. 2006, AJ, 132, 1354
Giese, R. H., Weiss, K., Zerull, R. H., & Ono, T. 1978, A&A, 65, 265
Girardi, L., Groenewegen, M. A. T., Hatziminaoglou, E., & da Costa, L. 2005, A&A, 436, 895
Grun, E., Zook, H. A., Fechtig, H., & Giese, R. H. 1985, Icar, 62, 244
Hauser, M., Kelsall, T., Leisawitz, D., & Weiland, J. 1998, COBE Diffuse Infrared Background Experiment (DIRBE) Explanatory Supplement
Hauser, M. G., Kelsall, T., Moseley, S. H. J., et al. 1991, in AIP Conf. Ser. 222, After the First Three Minutes, ed. S. S. Holt et al. (Melville, NY: AIP), 161
Jones, T. J., & Gehrz, R. D. 1990, AJ, 100, 274
Kelsall, T., Weiland, J. L., Franz, B. A., et al. 1998, ApJ, 508, 44
Lasue, J., Levasseur-Regourd, A.-C., & Renard, J.-B. 2020, P&SS, 190, 104973
Leinert, C., & Blanck, B. 1982, A&A, 105, 364
Leinert, C., Bowyer, S., Haikala, L. K., et al. 1998, A&AS, 127, 1
Levasseur-Regourd, A. C. 1996, in ASP Conf. Ser. 104, IAU Colloq. 150: Physics, Chemistry, and Dynamics of Interplanetary Dust, ed. B. A. S. Gustafson & M. S. Hanner (San Francisco, CA: ASP), 301
Liou, J. C., Dermott, S. F., & Xu, Y. L. 1995, P&SS, 43, 717
Lisse, C. M., Freudenreich, H. T., Hauser, M. G., et al. 1994, ApJL, 432, L71
Martin, P. G., & Whittet, D. C. B. 1990, ApJ, 357, 113
Matsumoto, T., Kawada, M., Murakami, H., et al. 1996, PASJ, 48, L47
Nagata, T. 1990, ApJL, 348, L13
Nesvorny, D., Janches, D., Vokrouhlicky, D., et al. 2011, ApJ, 743, 129
Nesvorny, D., Jenniskens, P., Levison, H. F., et al. 2010, ApJ, 713, 816
Pitz, E., Leinert, C., Schulz, A., & Link, H. 1979, A&A, 74, 15
Reach, W. T. 1988, ApJ, 335, 468
Sano, K., Matsuura, S., Yomo, K., & Takahashi, A. 2020, ApJ, 901, 112
Schramm, L. S., Brownlee, D. E., & Wheelock, M. M. 1989, Metic, 24, 99
Silverberg, R. F., Scholl, M. S., Hauser, M. G., et al. 1993, Proc. SPIE, 2019, 180
Skrutskie, M. F., Cutri, R. M., Stiening, R., et al. 2006, AJ, 131, 1163
Soderblom, L. A., Becker, T. L., Bennett, G., et al. 2002, Sci, 296, 1087
Sparrow, J. C., & Ney, E. P. 1972, ApJ, 174, 705
Takimoto, K., Arai, T., Matsuura, S., et al. 2022, ApJ, 926, 6
Tsumura, K., Battle, J., Bock, J., et al. 2010, ApJ, 719, 394
Tsumura, K., Matsumoto, T., Matsuura, S., et al. 2013, PASJ, 65, 1207
Van de Noord, E. L. 1970, ApJ, 161, 309
Weinberg, J. L., & Hahn, R. C. 1980, in Solid Particles in the Solar System; Proc.of the Symp., ed. I. Halliday & B. A. McIntosh (Dordrecht: Reidel), 19
Wolstencroft, R. D., & Brandt, J. C. 1967, NASSP, 150, 57
Yang, H., & Ishiguro, M. 2015, ApJ, 813, 87